

# Evaluation of single crystal elastic stiffness coefficients of a nickel-based superalloy by electron backscatter diffraction and nanoindentation

Joris Everaerts<sup>a</sup>, Chrysanthi Papadaki<sup>a</sup>, Wei Li<sup>b</sup>, Alexander M. Korsunsky<sup>a</sup>

<sup>a</sup> Department of Engineering Science, University of Oxford, Parks Road, Oxford OX1 3PJ, UK

<sup>b</sup> Rolls-Royce plc., Elton Road, Derby DE24 8ED, UK

Corresponding author

Professor Alexander M. Korsunsky

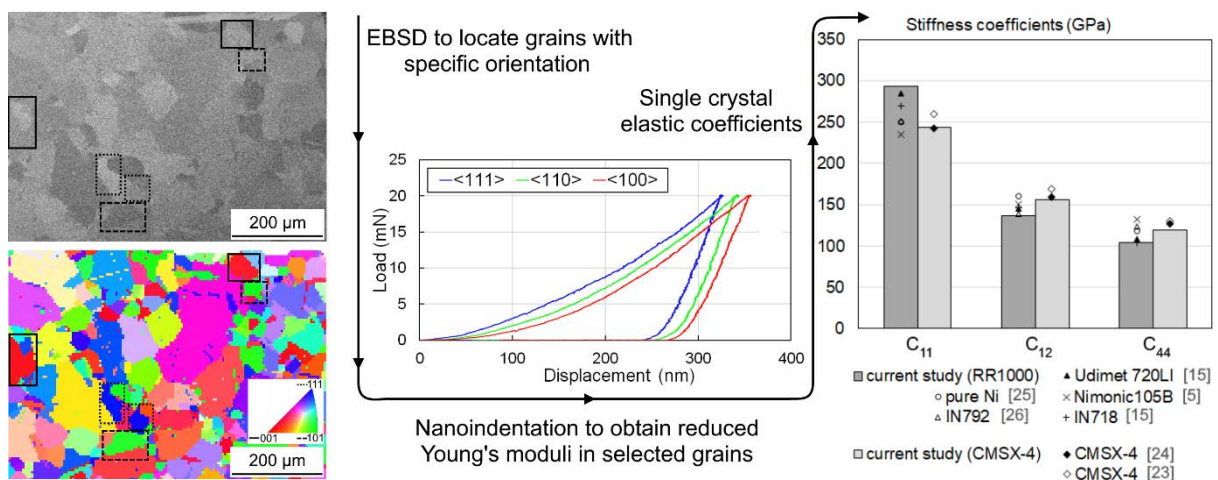
[alexander.korsunsky@eng.ox.ac.uk](mailto:alexander.korsunsky@eng.ox.ac.uk)

Tel. +44 1865 2 73043

E-mail addresses of other authors

[joris.everaerts@eng.ox.ac.uk](mailto:joris.everaerts@eng.ox.ac.uk); [chrysanthi.papadaki@eng.ox.ac.uk](mailto:chrysanthi.papadaki@eng.ox.ac.uk); [Wei.Li@Rolls-Royce.com](mailto:Wei.Li@Rolls-Royce.com)

## Graphical abstract



## Abstract

A new methodology was developed in order to obtain single crystal elastic coefficients from nanoindentation experiments on a cubic polycrystal. The method consists of locating grains that are oriented with a  $\langle 100 \rangle$ ,  $\langle 110 \rangle$  or  $\langle 111 \rangle$  direction near-parallel to the sample surface normal by means of electron backscattering diffraction. The reduced Young's moduli of the selected grains are then determined by nanoindentation. Finally, the average reduced modulus and Euler angles of each grain are used as input for a least-squares optimisation to calculate the three independent stiffness coefficients, which can then be used to obtain Young's modulus in any crystallographic direction. This technique, which was validated on a single crystal nickel-based superalloy (CMSX-4) with known elastic coefficients, was applied to a polycrystalline nickel-based superalloy (RR1000) with unknown elastic coefficients, resulting in a correct prediction of the general trend of increasing Young's modulus from the  $\langle 100 \rangle$  to the  $\langle 110 \rangle$  to the  $\langle 111 \rangle$  direction. The stiffness coefficients  $C_{11}$ ,  $C_{12}$  and  $C_{44}$  were found to be 282, 121 and 108 GPa, respectively. These results, which are representative of the  $\gamma/\gamma'$  structure as a whole, are in good agreement with literature data on similar superalloys. By constructing a visual representation of the elastic anisotropy based on the crystallographic factor, it is shown that the observed anisotropy is lower compared to other alloys.

**Keywords:** Nanoindentation; Electron backscattering diffraction (EBSD); Nickel alloys; Elastic behaviour

# 1 Introduction

The pursuit to improve the energy efficiency of turbine engines is driving the ongoing development of new nickel-based superalloys with improved temperature capability [1]. Rapid evaluation of mechanical properties using limited amounts of material is necessary to support this development [2]. The mechanical properties of these alloys are strongly influenced by the presence of coherent  $\gamma'$  precipitates in the face-centred cubic (f.c.c.)  $\gamma$  matrix and by the overall chemical composition. Moreover, the shape and size distribution of  $\gamma'$  precipitates can be controlled by changing the composition and by heat treatments [3]. Given the fact that nickel-based superalloys often contain more than ten different alloying elements, [1] the relationship between composition, microstructure and mechanical properties is tremendously complex. For example, changes in composition are known to have a strong effect on the direction-dependent Young's moduli of both the  $\gamma$  and the  $\gamma'$  phases [4–7].

Young's modulus for a specific crystallographic direction can be derived from the elastic stiffness coefficients by Hooke's law. For a material with a cubic crystal structure the anisotropic elastic behaviour is characterised by three independent elastic coefficients  $C_{11}$ ,  $C_{12}$  and  $C_{44}$ , [8] and Hooke's law takes the following form using Voigt notation:

$$\begin{bmatrix} \sigma_1 \\ \sigma_2 \\ \sigma_3 \\ \sigma_4 \\ \sigma_5 \\ \sigma_6 \end{bmatrix} = \begin{bmatrix} C_{11} & C_{12} & C_{12} & 0 & 0 & 0 \\ & C_{11} & C_{12} & 0 & 0 & 0 \\ & & C_{11} & 0 & 0 & 0 \\ & & & C_{44} & 0 & 0 \\ & & & & C_{44} & 0 \\ & & & & & C_{44} \end{bmatrix} \begin{bmatrix} \varepsilon_1 \\ \varepsilon_2 \\ \varepsilon_3 \\ \varepsilon_4 \\ \varepsilon_5 \\ \varepsilon_6 \end{bmatrix}$$

*symm*

The elastic stiffness coefficients can be measured from single crystal specimens using photoacoustic techniques such as Brillouin light scattering [9–12] or picosecond

ultrasonics [13,14]. However, measuring single crystal elastic stiffness coefficients from polycrystalline bulk specimens is not straightforward. One possibility is to combine neutron diffraction experiments with in-situ tensile or compression testing, which allows for the determination of the lattice strain response for multiple reflections, each corresponding to ensemble averages from groups of grains that have a certain orientation with respect to the loading direction. The plane-specific modulus can then be calculated from each reflection [15]. However, because of texture and neighbouring grain effects it is necessary to apply Reuss or Voigt averaging in order to calculate the elastic stiffness coefficients from the lattice strain data.

A more direct way to evaluate the elastic behaviour of anisotropic materials has been reported by Vlassak et al. [16,17] and involves indentation experiments to determine the indentation modulus. They derived a rigorous analytical method, based on earlier work by Willis [18], to calculate the indentation modulus for any orientation, using the stiffness coefficients as input and assuming that the contact area between the indenter and the surface is either circular or elliptical [17]. A numerical adaptation to this method, which allows implementing a triangular indenter shape, resulted in theoretical indentation moduli that were in close agreement with indentation moduli obtained from experiments on single crystals [16]. Although this illustrates that indentation experiments are sensitive to the orientation of the material, the method does not solve the inverse problem, i.e. determining unknown stiffness coefficients from the indentation moduli. Furthermore, the situation becomes more complicated when investigating polycrystalline materials instead of single crystals.

The purpose of this paper is to present a new and faster methodology to measure direction-dependent moduli and elastic stiffness coefficients based on electron backscatter diffraction (EBSD) and nanoindentation, which eliminates the need for

access to a synchrotron or neutron source. This method is applied to a polycrystalline nickel-based superalloy with unknown coefficients and validated using a single crystal nickel-based superalloy with known stiffness coefficients. However, it can also be used directly to investigate other cubic polycrystals. The results are compared to data from literature and an assessment of the validity of the method is made.

## 2 Material and methods

### 2.1 Experimental procedure

The polycrystalline nickel-based superalloy that was investigated in this study is coarse-grained RR1000, which has a nominal composition as shown in Table 1. The sample was mounted in epoxy resin, ground and polished using colloidal silica. This was followed by electrochemical polishing for 5 minutes at 50 A/dm<sup>2</sup> in an electrolyte containing 20 vol.% sulphuric acid in absolute methanol [19]. Scanning electron microscope (SEM) imaging and grain orientation mapping by EBSD was performed using a Tescan LYRA3 SEM equipped with an Oxford Instruments NordlysNano detector. This allowed for the identification of grains with a <100>, <110> or <111> direction near-parallel to the sample surface normal. Four grains of each orientation were selected for nanoindentation analysis and demarcated by a rectangle that was milled using a focused ion beam. This allowed for the grains to be located more easily once the sample was mounted on the nanoindenter stage.

<b>wt.%</b>	<b>Ni</b>	<b>Cr</b>	<b>Co</b>	<b>Mo</b>	<b>Al</b>	<b>Ti</b>	<b>Ta</b>	<b>C</b>	<b>B</b>	<b>Zr</b>	<b>Hf</b>
<b>RR1000</b>	<i>bal</i>	15	18.5	5	3	3.6	2	0.027	0.015	0.06	0.5

Table 1. Nominal composition of RR1000 alloy [20]

Three indentations were performed in-situ in each grain using an Alemnis Nanoindenter with a diamond Berkovich tip (Synton-MDP), making sure that the

distance between each indentation as well as the distance to the nearest grain boundary was at least three times the size of an indentation. Each indentation was load-controlled and consisted of a load increase at 0.2 mN/s to a maximum load of 20 mN, a hold period of 20s, and a load decrease at 0.2 mN/s. Each unloading curve was analysed by means of Oliver and Pharr's method, [21] which involves least-squares fitting of a simple power law to the load-displacement data. After analytical differentiation the unloading slope  $S$  at peak load was evaluated and used to calculate the experimental reduced modulus  $E_r^{exp}$  from the following equation: [21]

$$S - S_F = \frac{2}{\sqrt{\pi}} \beta E_r^{exp} \sqrt{A} \quad (1)$$

The frame stiffness  $S_F$  was determined after five indentations on a calibrated fused silica sample with known modulus. The contact area  $A$  was obtained from the contact depth  $h_c$  assuming a perfect Berkovich tip, which means that  $A = 24.5h_c^2$  and the correction factor  $\beta = 1.05$  [22].

## 2.2 Optimisation procedure to obtain stiffness coefficients

For each grain, the average experimental reduced modulus obtained from three indentations was used as input for a least-squares optimisation to calculate the independent stiffness coefficients  $C_{11}$ ,  $C_{12}$  and  $C_{44}$ . The Euler angles, determined by EBSD, were also used in order to describe the exact orientation of each probed grain. The optimisation procedure consists of minimizing the sum of squared differences,  $D$ , between the experimentally determined average reduced modulus  $E_{r,j}^{exp}$  and the calculated reduced modulus  $E_{r,j}^{fit}$  for each grain  $j$ :

$$D = \sum_{j=1}^n (E_{r,j}^{exp} - E_{r,j}^{fit})^2 \quad (2)$$

This iterative procedure was implemented in MATLAB® using the optimisation tool and the open source MTEX toolbox (version 4.5.0).  $D$  was minimized by means of the *fsolve* function (Levenberg-Marquardt algorithm), with  $C_{11}$ ,  $C_{12}$  and  $C_{44}$  as unconstrained variables. The starting point values for  $C_{11}$ ,  $C_{12}$  and  $C_{44}$  were 284.9, 144.9 and 108.9 GPa, respectively [15]. During each iteration, the calculated reduced modulus,  $E_{r,j}^{fit}$ , was obtained for each grain  $j$  by using the following equation: [21]

$$\frac{1}{E_{r,j}^{fit}} = \frac{(1-\nu_j^2)}{E_j^{fit}} + \frac{(1-\nu_i^2)}{E_i} \quad (3)$$

The values used for the elastic modulus  $E_i$  and Poisson's ratio  $\nu_i$  of the diamond indenter were 1141 GPa and 0.07, respectively [21]. The calculated modulus  $E_j^{fit}$  was obtained from the Euler angles of grain  $j$  and the current set of stiffness coefficients  $C_{11}$ ,  $C_{12}$  and  $C_{44}$  using the MTEX *Youngsmodulus* function. Parameter  $\nu_j$  represents the average in-plane Poisson's ratio for grain  $j$ . This was calculated by using the MTEX *PoissonRatio* function to obtain values for Poisson's ratio for in-plane directions between 0° and 180° in angular steps of 10°, with respect to the loading direction perpendicular to the sample surface, and averaging them. This function requires the stiffness coefficients as input, as well as the vectors describing the loading direction and in-plane directions, which were calculated based on the Euler angles of grain  $j$ . Using the average in-plane Poisson's ratio is a simplified approach, which was chosen because the in-plane orientation of the indenter is unknown. A more rigorous approach would require a detailed description of the contact between the material and the triangular Berkovich indenter, including the in-plane orientation of the indenter. The consequence of using the average in-plane Poisson's ratio is expected to be minimal, as will be discussed further below. As can be observed from equation (2), the

optimisation procedure incorporates all measurements, i.e. in multiple grains of different orientation, to simultaneously obtain all three stiffness coefficients. This way the influence of scatter, associated with individual nanoindentation measurements, on the final result is reduced.

### 2.3 Validation

The method described above was validated on CMSX-4, which is a single crystal nickel-based superalloy for which the elastic stiffness coefficients have been reported in literature [23,24]. The crystallographic orientation of the CMSX-4 specimen was first identified by EBSD. Based on this information, three samples were cut from the specimen using a water-cooled wheel cutting machine, in order to specifically obtain a  $\langle 100 \rangle$ ,  $\langle 110 \rangle$  or  $\langle 111 \rangle$  direction near-parallel to the sample surface normal. For each of the three samples, the Euler angles were then determined by EBSD and the average reduced modulus was obtained from five indentations. This input was used in the procedure described above to determine the stiffness coefficients  $C_{11}$ ,  $C_{12}$  and  $C_{44}$ .

## 3 Results and discussion

The microstructure of the RR1000 sample is shown in Figure 1 by low and high magnification SEM images. Figure 1a shows  $\gamma$  grains, which have an average grain diameter of 47  $\mu\text{m}$ , as determined by EBSD. It can also be observed that numerous twins are present. A higher magnification SEM image in Figure 1b shows secondary (in the range of hundreds of nanometres) and tertiary (in the range of tens of nanometres)  $\gamma'$  precipitates in the  $\gamma$  matrix [1]. The specific microstructure of this material has to be carefully considered when performing nanoindentation measurements. Firstly, special care has to be taken in order to avoid indentation of twins, because these have a different orientation with respect to the parent  $\gamma$  grain and



consequently would have a different response to indentation. Secondly, the size of  $\gamma'$  precipitates is in the nanometre range and thus well below the indent size achieved by nanoindentation, which is in the micrometre range. As a result, the properties measured by nanoindentation are those of the  $\gamma/\gamma'$  structure as a whole, without separating between  $\gamma$  and  $\gamma'$ . Additionally, it can be observed in Figure 1b that sample preparation by electrochemical polishing also caused slight etching of the  $\gamma'$  precipitates. However, the effect of this phenomenon on the indentation modulus is expected to be minimal, because the roughness due to etching is small (i.e. nanometre range) and the stiffness is evaluated from the unloading slope at peak load (i.e. at maximum indentation depth).

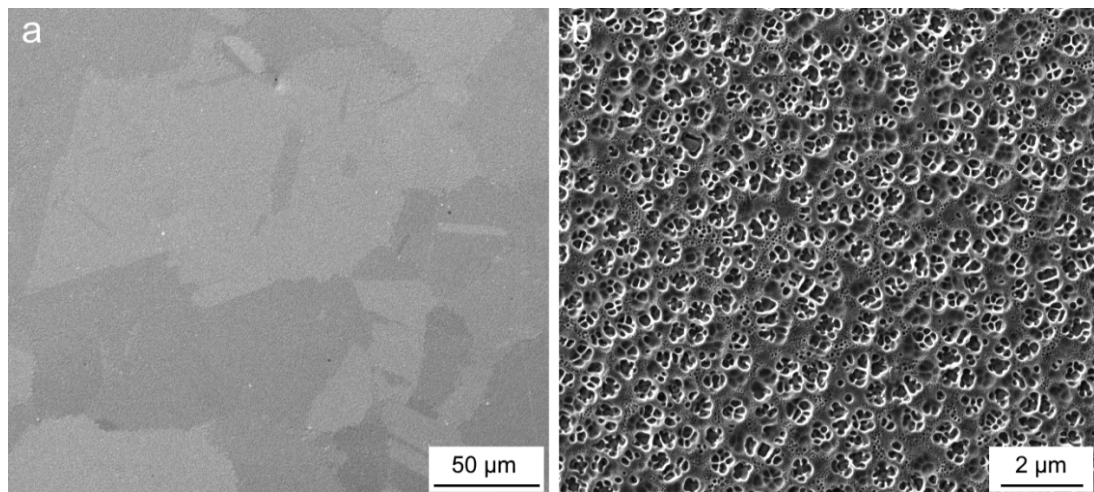


*Figure 1. SEM images of the RR1000 microstructure at low (a) and high (b) magnification*

The first step in the proposed methodology consists of locating grains that are oriented with a  $\langle 100 \rangle$ ,  $\langle 110 \rangle$  or  $\langle 111 \rangle$  direction near-parallel to the sample surface normal. This is illustrated in Figure 2, which shows SEM images (a,b) and inverse pole figure maps (c,d) at two different locations on the RR1000 sample surface. Four grains of each orientation were selected and highlighted in Figure 2 using solid, dashed and dotted lines for grains with a near- $\langle 100 \rangle$ ,  $\langle 110 \rangle$  or  $\langle 111 \rangle$  orientation, respectively. These grains were then demarcated by a rectangle that was milled using a focused

ion beam, allowing easy localisation after the sample was mounted on the nanoindenter stage. The misorientation angle between the surface normal and the desired direction ( $\langle 100 \rangle$ ,  $\langle 110 \rangle$  or  $\langle 111 \rangle$ ) ranged between 2.5 and 12.1 degrees for the chosen grains. However, the precise orientation of each grain, given by the Euler angles, is taken into account in the subsequent optimisation procedure as described in section 2.2.

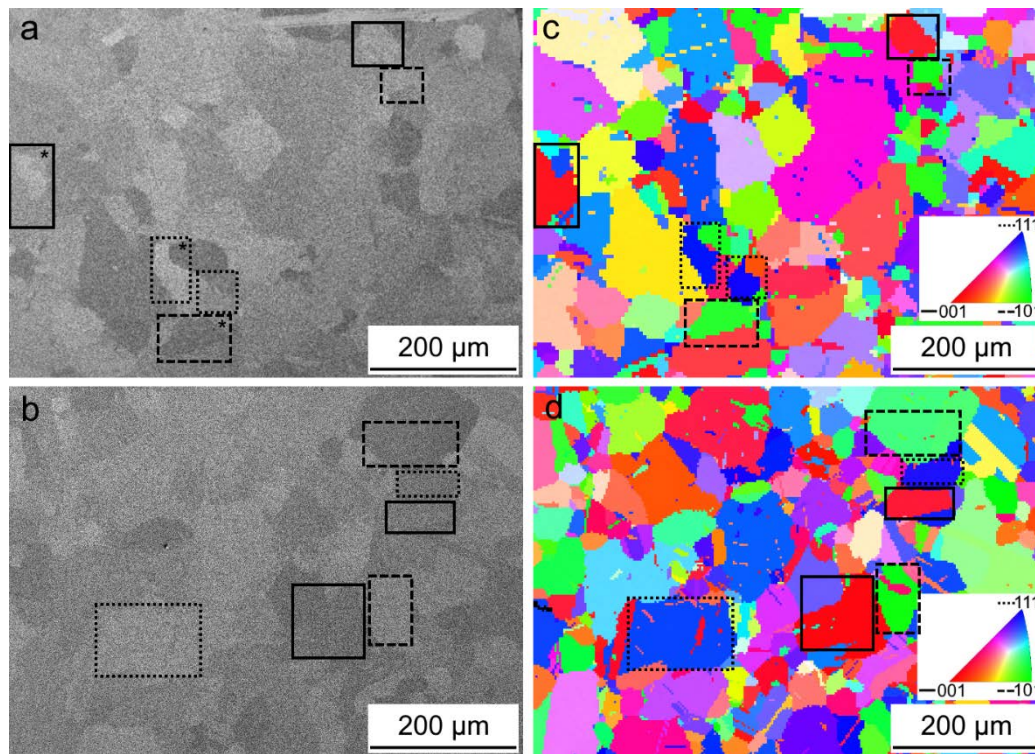


*Figure 2. a,b) SEM images of electropolished RR1000 surface highlighting the selected grains with near  $\langle 100 \rangle$ ,  $\langle 110 \rangle$  or  $\langle 111 \rangle$  orientation, and c,d) respective inverse pole figure maps (reference direction perpendicular to the paper)*

In order to illustrate the differences in nanoindentation response between grains with different orientations, the load-displacement curves of measurements in three selected grains are presented in Figure 3. The selected grains are marked by an asterisk symbol in Figure 2a. First of all, it can be observed that the maximum depth of indentation is lowest for the grain with near- $\langle 111 \rangle$  orientation and highest for the grain with near- $\langle 100 \rangle$  orientation. Given the fact that the hardness is equal to the peak

load divided by the projected area of contact at peak load [21], this means that the hardness is highest for the grain with near- $\langle 111 \rangle$  orientation and lowest for the grain with near- $\langle 100 \rangle$  orientation. Second of all, Figure 3 shows that the slope of the unloading curve is steeper for the grain with near- $\langle 111 \rangle$  orientation than for the grain with near- $\langle 110 \rangle$  orientation, which in turn is steeper compared to the unloading curve for the grain with near- $\langle 100 \rangle$  orientation. This illustrates that indenting grains with different orientations results in different unloading behaviour.

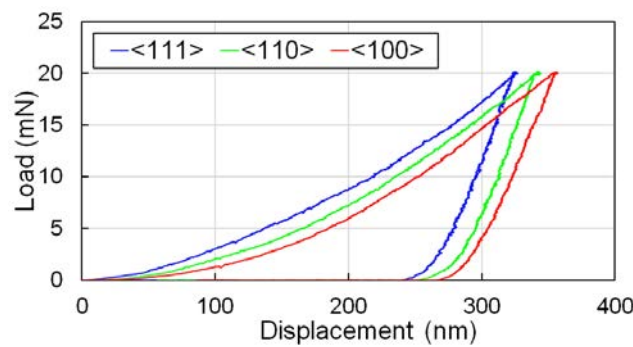


Figure 3. Load-displacement curves obtained from nanoindentation in alloy RR1000 for grains with near- $\langle 100 \rangle$ ,  $\langle 110 \rangle$  and  $\langle 111 \rangle$  orientation

Following Oliver and Pharr's method [21], the reduced Young's moduli  $E_r^{exp}$  were obtained from the load-displacement data. The results, which are presented in Figure 4, show the average  $E_r^{exp}$  for four grains of each approximate orientation, based on three indentations per grain. Consequently, a total of 36 nanoindentation measurements were performed. From these values and the Euler angles of each grain, the stiffness coefficients  $C_{11}$ ,  $C_{12}$  and  $C_{44}$  of alloy RR1000 were determined using the optimisation procedure described in section 2.2, and found to be 282, 121 and 108 GPa, respectively. The calculated Young's moduli in the  $\langle 100 \rangle$ ,  $\langle 110 \rangle$  and  $\langle 111 \rangle$  directions are 209, 250 and 268 GPa, respectively. In order to compare the calculated values with the experimental values, Figure 4 also shows the fitted reduced Young's moduli in the  $\langle 100 \rangle$ ,  $\langle 110 \rangle$  and  $\langle 111 \rangle$  directions, as obtained from equation

3. It can be observed that the results from the optimisation procedure provide a good fit and that the reduced Young's modulus follows the general trend of being lowest in the  $\langle 100 \rangle$  direction and highest in the  $\langle 111 \rangle$  direction.

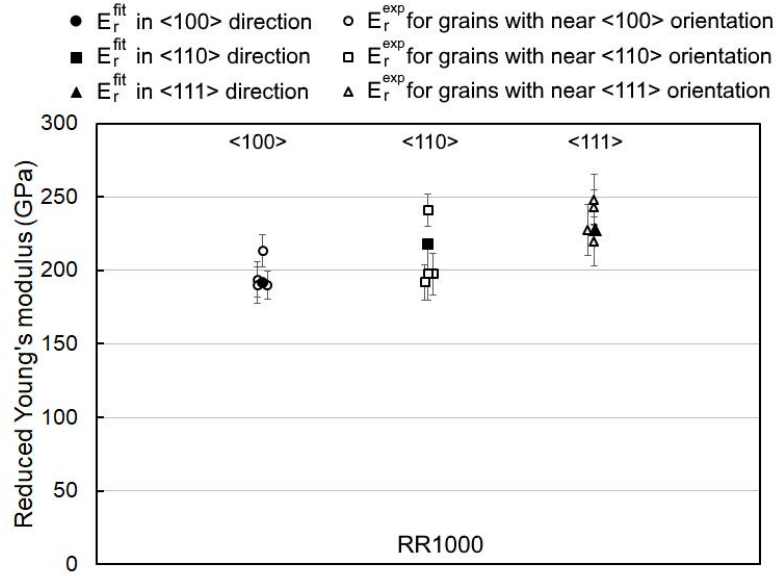


Figure 4. Experimentally determined reduced Young's moduli for grains in alloy RR1000 with near  $\langle 100 \rangle$ ,  $\langle 110 \rangle$  or  $\langle 111 \rangle$  orientations (open symbols), and fitted reduced Young's moduli in  $\langle 100 \rangle$ ,  $\langle 110 \rangle$  and  $\langle 111 \rangle$  directions (closed symbols)

In order to assess the validity of the proposed method, EBSD and nanoindentation measurements were also performed on single crystal alloy CMSX-4 as described in section 2.3. Figure 5 shows the average  $E_r^{exp}$  for each approximate orientation and the fitted reduced Young's moduli in the  $\langle 100 \rangle$ ,  $\langle 110 \rangle$  and  $\langle 111 \rangle$  directions, as obtained from the optimisation procedure. It should be noted that the misorientation angles between the surface normal and the desired directions ( $\langle 100 \rangle$ ,  $\langle 110 \rangle$  or  $\langle 111 \rangle$ ) were respectively 12.9, 9.5 and 18.4 degrees. The slightly higher misorientation of the sample with near- $\langle 111 \rangle$  orientation explains why the value for  $E_r^{exp}$  is lower than  $E_r^{fit}$  in the  $\langle 111 \rangle$  direction. However, the optimisation procedure takes this misorientation into account via the specific Euler angles of the actual

orientation of the sample. The stiffness coefficients  $C_{11}$ ,  $C_{12}$  and  $C_{44}$  for alloy CMSX-4 were found to be 243, 156 and 119 GPa, respectively.

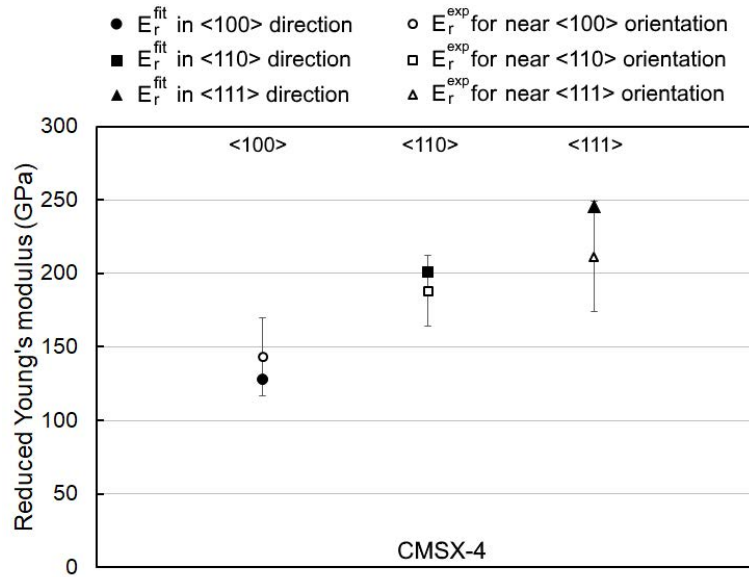


Figure 5. Experimentally determined reduced Young's moduli for CMSX-4 samples with near <100>, <110> or <111> orientation (open symbols), and fitted reduced Young's moduli in <100>, <110> and <111> directions (closed symbols)

The obtained results can now be compared with values found in literature. Figure 6 shows the stiffness coefficients  $C_{11}$ ,  $C_{12}$  and  $C_{44}$  and Young's moduli in the <100>, <110>, and <111> directions obtained for alloys CMSX-4 and RR1000 in this study and for various other nickel-based superalloys reported in literature [5,15,23–26]. It can be observed that for all of these alloys  $C_{11}$  is the stiffness coefficient with the largest value, followed by  $C_{12}$  and  $C_{44}$ , and Young's modulus is highest in the <111> direction and lowest in the <100> direction. The values obtained for CMSX-4 are in good agreement with those reported in literature [23,24]. For example,  $C_{11}$ ,  $C_{12}$  and  $C_{44}$  only differ by respectively 0.3%, 1.8% and 5.8% from the coefficients reported by Zhang et al. [24], which were obtained by surface Brillouin scattering. The values obtained for RR1000 show the same trend and are in line with the literature data, in particular with alloys Udimet 720LI and IN718 [15]. The agreement with alloy Udimet 720LI is not entirely surprising, given the fact that both alloys are relatively similar in



terms of composition [1,27]. However, with respect to the literature values,  $C_{12}$  and  $C_{44}$  correspond to the lower range, whereas  $C_{11}$  defines the upper limit. In terms of directional Young's moduli, it can be observed that, even though the general trend is predicted correctly, the differences between the directions are less pronounced for RR1000 in comparison to what has been reported in literature. The smaller differences between the directional Young's moduli can be related to the stiffness coefficients in a straightforward manner by evaluating the Zener ratio for anisotropy  $A$ , which for cubic materials is defined as [28]:

$$A = \frac{2C_{44}}{C_{11} - C_{12}}. \quad (4)$$

The anisotropy ratio obtained for the RR1000 alloy used in this study is approximately 1.33, which is smaller compared to the other alloys shown in Figure 6 because  $C_{44}$  is smaller and the difference between  $C_{11}$  and  $C_{12}$  is larger. Consequently, the material is apparently less anisotropic and the differences between Young's moduli in different directions are smaller. For alloy CMSX-4, the observed anisotropy ratio is approximately 2.7, which is similar to what has been reported in literature for the same alloy [23,24].

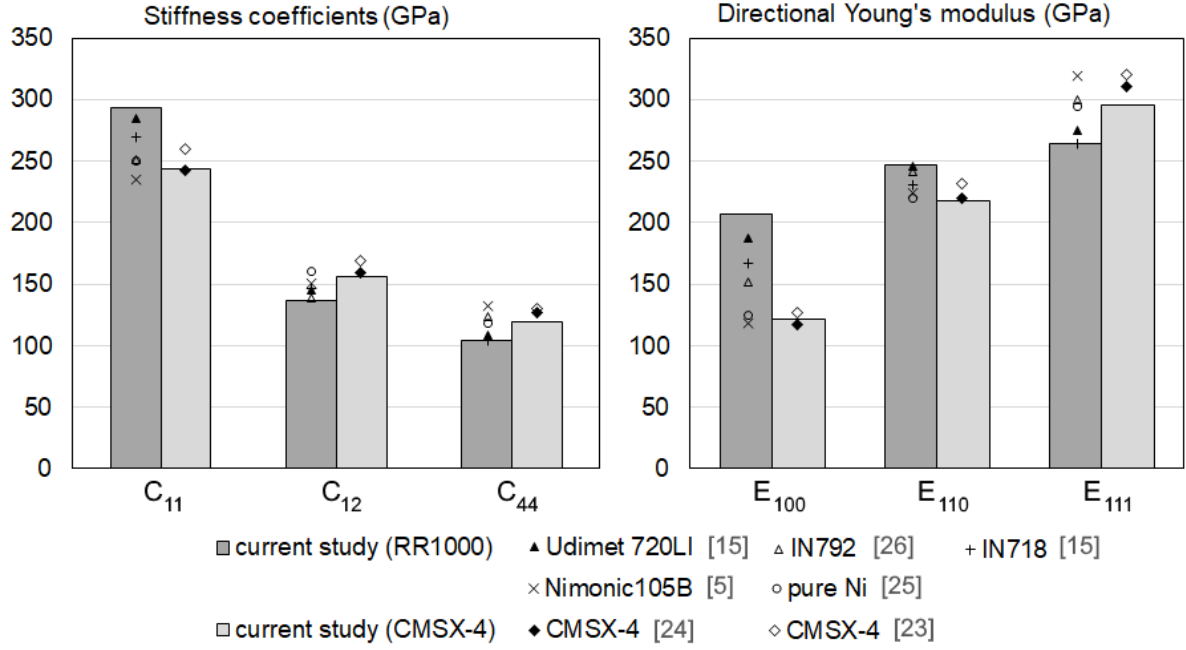


Figure 6. Comparison of stiffness coefficients  $C_{11}$ ,  $C_{12}$  and  $C_{44}$  and Young's moduli in the  $\langle 100 \rangle$ ,  $\langle 110 \rangle$  and  $\langle 111 \rangle$  directions with various alloys from literature

It is also convenient to visualise the anisotropy by using an approach that is based on the crystallographic factor  $\Gamma_{hkl}$ , which is defined as [29]:

$$\Gamma_{hkl} = \frac{h^2 k^2 + h^2 l^2 + k^2 l^2}{(h^2 + k^2 + l^2)^2} \quad (5)$$

It can be shown that the inverse of Young's modulus  $E_{hkl}$  in direction  $\langle hkl \rangle$  is linearly dependent with  $\Gamma_{hkl}$  as follows [15,29]:

$$E_{hkl}^{-1} = S_{11} - 2 \left( S_{11} - S_{12} - \frac{1}{2} S_{44} \right) \Gamma_{hkl} \quad (6)$$

In this equation,  $S_{11}$ ,  $S_{12}$  and  $S_{44}$  represent components of the compliance matrix. Note that, because the compliance matrix is the inverse of the stiffness matrix, these compliance coefficients can be evaluated for cubic materials as:

$$S_{11} = \frac{C_{11} + C_{12}}{(C_{11} - C_{12})(C_{11} + 2C_{12})} \quad (7)$$

$$S_{12} = \frac{-C_{12}}{(C_{11} - C_{12})(C_{11} + 2C_{12})} \quad (8)$$

$$S_{44} = \frac{1}{C_{44}} \quad (9)$$

Moreover, the ratio of Poisson's ratio  $\nu_{hkl}$  to  $E_{hkl}$  in direction  $\langle hkl \rangle$  is also linearly dependent with  $\Gamma_{hkl}$  [15]:

$$-\frac{\nu_{hkl}}{E_{hkl}} = \frac{1}{2(C_{11} + 2C_{12})} - \frac{1}{2}S_{11} + \left(S_{11} - S_{12} - \frac{1}{2}S_{44}\right)\Gamma_{hkl} \quad (10)$$

Using equations (6) and (10), the data presented in Figure 6 can be plotted as a function of  $\Gamma_{hkl}$ . Figure 7a and b shows respectively  $E_{hkl}$  and  $-\nu_{hkl}/E_{hkl}$  for alloys CMSX-4 and RR1000 (this study) and for several other alloys reported in literature. The data points represent the values in directions  $\langle 100 \rangle$  ( $\Gamma_{hkl}=0$ ),  $\langle 110 \rangle$  ( $\Gamma_{hkl}=1/4$ ), and  $\langle 111 \rangle$  ( $\Gamma_{hkl}=1/3$ ). These plots demonstrate the linearity as described by equations (6) and (7). It can be observed that the results for CMSX-4 are in close agreement with literature data [23,24]. The results for RR1000 follow the same general trend as other alloys, although the slope is less steep. The slope represents the variation of Young's modulus in different crystallographic directions. In order to relate this to the Zener anisotropy ratio  $A$ , equation (4) can be rewritten in terms of the compliance coefficients:

$$A = \frac{2C_{44}}{C_{11} - C_{12}} = \frac{2(S_{11} - S_{12})}{S_{44}} \quad (11)$$

This definition of  $A$  can then be used to rewrite equations (6) and (10) as follows:

$$E_{hkl}^{-1} = S_{11} - S_{44}(A - 1)\Gamma_{hkl} \quad (12)$$



$$-\frac{\nu_{hkl}}{E_{hkl}} = S_{12} + \frac{S_{44}(A-1)}{2} \Gamma_{hkl} \quad (13)$$

Equations (12) and (13) show that for each alloy the intercept at  $\Gamma_{hkl}=0$  is equal to  $S_{11}$  in Figure 7a and  $S_{12}$  in Figure 7b, and the slope is equal to  $-S_{44}(A-1)$  in Figure 7a and  $\frac{S_{44}(A-1)}{2}$  in Figure 7b. Hence, these plots provide a complete visual representation of the elastic anisotropy of the various alloys. Additionally, this shows that a smaller anisotropy ratio leads to a shallower slope in both plots. In case of isotropy,  $A$  would be equal to one, which means that the slope would be zero and Young's modulus would logically be the same in every direction. This visual representation confirms that the anisotropy observed for RR1000 in this study is smaller compared to the anisotropy of other nickel-based superalloys reported in literature.

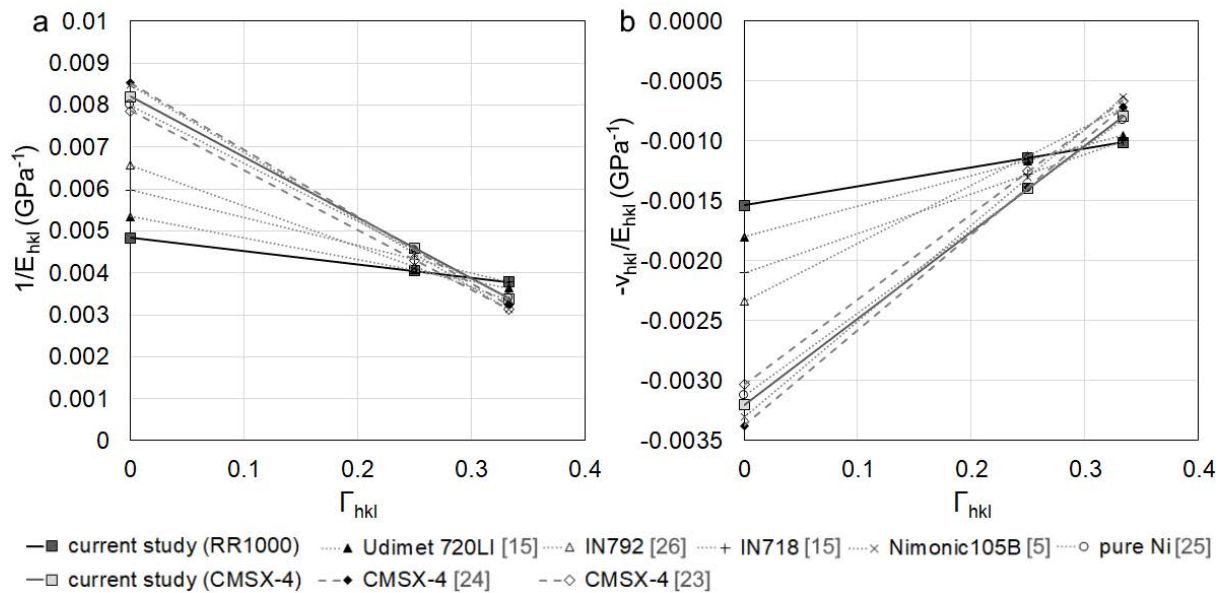


Figure 7. Inverse Young's modulus  $E_{hkl}$  (a) and ratio of Poisson's ratio to Young's modulus  $-\nu_{hkl}/E_{hkl}$  (b) as a function of the crystallographic factor  $\Gamma_{hkl}$  for results obtained in the current study (CMSX-4 and RR1000) and for various alloys in literature

Based on the comparison with literature data, it is necessary to reflect on possible reasons why the observed anisotropy of RR1000 is smaller. Either the studied alloy

does indeed exhibit lower anisotropy compared to other nickel-based superalloys, or the methodology that was used to determine the stiffness coefficients leads to an underestimation of the anisotropy. To the author's knowledge, the stiffness coefficients or directional Young's moduli of RR1000 have not yet been reported elsewhere. Therefore, it is only possible to qualitatively assess whether the anisotropy could be lower compared to other alloys. As already mentioned, due to the fine dispersion of  $\gamma'$  precipitates the stiffness measured by nanoindentation is that of the  $\gamma/\gamma'$  structure as a whole. Ma et al. [6] measured individual stiffness coefficients for the  $\gamma$  and  $\gamma'$  phases in alloy CM 247 LC by neutron diffraction, which show that the  $\gamma'$  phase behaves less anisotropic compared to the  $\gamma$  phase. Additionally, a similar experiment on single-crystal alloy CMSX-4 showed that the elastic modulus in the  $\langle 100 \rangle$  direction is larger for the  $\gamma'$  phase compared to the  $\gamma$  phase [4]. Because the stiffness coefficients are known to be different for the  $\gamma$  and  $\gamma'$  phase, it is logical that the  $\gamma'$  volume fraction would affect the effective elastic moduli of the  $\gamma/\gamma'$  structure. In terms of chemical composition, alloy RR1000 is relatively close Udimet 720LI. Accordingly, the stiffness properties of Udimet 720LI are the closest to those observed for RR1000 in this study (see Figure 6 and Figure 7), and the lower anisotropy ratio for RR1000 could be a result of its higher  $\gamma'$  volume fraction [27]. Furthermore, the effective modulus is not only dependent on the stiffness coefficients of the  $\gamma$  and  $\gamma'$  phase, but also on the  $\gamma'$  precipitate morphology and distribution. This can be understood by considering that a geometric constraint is imposed by each phase, which also affects the apparent elastic and plastic anisotropy [4,6].

Although the results obtained for CMSX-4 and RR1000 are in close agreement with literature and the differences can be explained rationally, it is useful to consider possible sources of error in the proposed experimental methodology. First of all, the

calculated reduced Young's moduli that are used in the least squares optimisation procedure are obtained from Young's moduli by using equation 3. This requires knowledge of Poisson's ratio  $\nu_j$  for grain  $j$ . As described in section 2.2,  $\nu_j$  in this case was chosen to represent the average in-plane Poisson's ratio for grain  $j$ . This is an isotropic approximation due to the fact that, when using a triangular indenter (i.e. Berkovich) for indenting an anisotropic material, it can be expected that the indentation modulus depends on the orientation of the indenter. The relation between indentation modulus and Young's modulus is consequently more complicated. However, Vlassak and Nix [16] reported that the variation of the modulus with the in-plane orientation of the indenter is negligible, which means that the simplification of using an average in-plane Poisson's ratio is justifiable and should not have a significant effect on the results. Nonetheless, a more rigorous optimisation procedure could be constructed by implementing the anisotropic method proposed by Vlassak et al. [16,17] to calculate the reduced Young's moduli more accurately for each iteration step. This would drastically increase the complexity and thus computation time of this procedure, but could potentially further improve the accuracy of the results. Second of all, the studied RR1000 sample is a polycrystal, and therefore the grains selected for indentation are surrounded and supported by their neighbouring grains. During indentation the compliance of the surrounding grain structure may reduce the sensitivity of the measurement to the orientation of the indented grain, which could potentially explain the lower observed anisotropy. However, this effect should be minimal because the indent size, which is in the order of a few micrometres, is much smaller than the average grain size of 47  $\mu\text{m}$ . Special care was also taken to avoid indenting too close to grain boundaries or twins. Nevertheless, this poses a limit on which materials can be analysed by the proposed method, because the grain size should be sufficiently

large in order to minimise the influence of neighbouring grains. Finally, the nanoindentation data were not corrected for possible pileup effects, which could lead to errors. However, the tendency for pileup to occur is not very strong for work-hardening metals such as nickel-based superalloys, and thus the errors on the experimental reduced moduli are not expected to be significant [30].

In summary, the proposed methodology of EBSD, nanoindentation and a least-squares optimisation can be used to obtain elastic stiffness coefficients from a polycrystalline material. In the current case, i.e. for nickel-based superalloys, these are representative of the  $\gamma/\gamma'$  structure as a whole, which means that they may be used to calculate effective Young's moduli in any direction. The method is applicable to any cubic material, provided that the grain size is sufficiently larger with respect to the indent size.

## 4 Conclusions

A new methodology was proposed in order to measure single crystal elastic stiffness coefficients and direction-dependent moduli from a polycrystalline material. The method consists of:

- EBSD mapping of a specific area on the polished sample surface
- Localisation of grains with a  $\langle 100 \rangle$ ,  $\langle 110 \rangle$  or  $\langle 111 \rangle$  direction near-parallel to the sample surface normal
- *In situ* nanoindentation experiments in the selected grains to obtain the average reduced Young's modulus for each grain
- Least-squares optimisation, using the reduced moduli and corresponding Euler angles as input, to obtain the independent stiffness coefficients

This method, which was validated on a single crystal nickel-based superalloy (CMSX-4), was applied to polycrystalline nickel-based superalloy RR1000. The stiffness coefficients  $C_{11}$ ,  $C_{12}$  and  $C_{44}$  were found to be 282, 121 and 108 GPa, respectively. The Young's moduli in the  $\langle 100 \rangle$ ,  $\langle 110 \rangle$  and  $\langle 111 \rangle$  directions were 209, 250 and 268 GPa, respectively. The obtained values describe the effective moduli of the  $\gamma/\gamma'$  structure as a whole, and are in close agreement with literature data on similar nickel-based superalloys. The anisotropy ratio, however, is smaller compared to other alloys, which could be due to the higher volume fraction and different morphology and distribution of the  $\gamma'$  precipitates.

## References

- [1] R.C. Reed, The Superalloys fundamentals and applications, Cambridge University Press, 2006. doi:10.1017/CBO9780511541285.
- [2] A.A.N. Németh, D.J. Crudden, D.M. Collins, D.E.J. Armstrong, R.C. Reed, Novel techniques to assess environmentally-assisted cracking in a Nickel-based superalloy, in: Superalloys 2016: Proceedings of the 13th International Symposium on Superalloys, Wiley-Blackwell, 2016: pp. 801–810. doi:10.1002/9781119075646.ch86.
- [3] G.P. Sabol, R. Stickler, Microstructure of Nickel-Based Superalloys, *Physica Status Solidi (B)*. 35 (1969) 11–52. doi:10.1002/pssb.19690350102.
- [4] D. Dye, J. Coakley, V.A. Vorontsov, H.J. Stone, R.B. Rogge, Elastic moduli and load partitioning in a single-crystal nickel superalloy, *Scripta Materialia*. 61 (2009) 109–112. doi:10.1016/j.scriptamat.2009.03.008.
- [5] F. Wallow, G. Neite, W. Schröer, E. Nembach, Stiffness constants, dislocation

- line energies, and tensions of Ni<sub>3</sub>Al and of the  $\gamma'$ -phases of NIMONIC 105 and of NIMONIC PE16, *Physica Status Solidi (A)*. 99 (1987) 483–490. doi:10.1002/pssa.2210990218.
- [6] S. Ma, D. Brown, M.A.M. Bourke, M.R. Daymond, B.S. Majumdar, Microstrain evolution during creep of a high volume fraction superalloy, *Materials Science and Engineering A*. 399 (2005) 141–153. doi:10.1016/j.msea.2005.02.034.
- [7] H. Yasuda, T. Takasugi, M. Koiwa, Elasticity of Ni-based L12-type intermetallic compounds, *Acta Metallurgica et Materialia*. 40 (1992) 381–387. doi:10.1016/0956-7151(92)90312-3.
- [8] G.E. Dieter, *Mechanical metallurgy*, McGraw-Hill Book Company, New York, 1962. doi:10.1016/S0016-0032(62)91145-6.
- [9] C. Sanchez-Valle, S. V Sinogeikin, Z.A.D. Lethbridge, R.I. Walton, C.W. Smith, K.E. Evans, J.D. Bass, Brillouin scattering study on the single-crystal elastic properties of natrolite and analcime zeolites, *Journal of Applied Physics*. 98 (2005) 53508. doi:10.1063/1.2014932.
- [10] T. Wittkowski, G. Distler, K. Jung, B. Hillebrands, J.D. Comins, General methods for the determination of the stiffness tensor and mass density of thin films using Brillouin light scattering: Study of tungsten carbide films, *Physical Review B*. 69 (2004) 205401-1-205401–9.
- [11] R.E. Benner, E.M. Brody, H.R. Shanks, Elastic moduli of ReO<sub>3</sub> by Brillouin scattering, *Journal of Solid State Chemistry*. 22 (1977) 361–366. doi:10.1016/0022-4596(77)90012-3.
- [12] S. V. Sinogeikin, D.L. Lakshtanov, J.D. Nicholas, J.M. Jackson, J.D. Bass, High

- temperature elasticity measurements on oxides by Brillouin spectroscopy with resistive and IR laser heating, *Journal of the European Ceramic Society*. 25 (2005) 1313–1324. doi:10.1016/j.jeurceramsoc.2005.01.001.
- [13] H. Ogi, N. Nakamura, M. Hirao, Picosecond ultrasound spectroscopy for studying elastic modulus of thin films: a review, *Nondestructive Testing and Evaluation*. 26 (2011) 267–280. doi:10.1080/10589759.2011.569027.
- [14] T. Lee, K. Ohmori, C.S. Shin, D.G. Cahill, I. Petrov, J.E. Greene, Elastic constants of single-crystal  $\text{TiN}_x(001)$  ( $0.67 < x < 1.0$ ) determined as a function of  $x$  by picosecond ultrasonic measurements, *Physical Review B*. 71 (2005) 144106-1-144106–6.
- [15] P.E. Aba-Perea, T. Pirling, P.J. Withers, J. Kelleher, S. Kabra, M. Preuss, Determination of the high temperature elastic properties and diffraction elastic constants of Ni-base superalloys, *Materials and Design*. 89 (2016) 856–863. doi:10.1016/j.matdes.2015.09.152.
- [16] J.J. Vlassak, W.D. Nix, Measuring the elastic properties of anisotropic materials by means of indentation experiments, *Journal of the Mechanics and Physics of Solids*. 42 (1994) 1223–1245. doi:10.1016/0022-5096(94)90033-7.
- [17] J.J. Vlassak, M. Ciavarella, J.R. Barber, X. Wang, The indentation modulus of elastically anisotropic materials for indenters of arbitrary shape, *Journal of the Mechanics and Physics of Solids*. 51 (2003) 1701–1721. doi:10.1016/S0022-5096(03)00066-8.
- [18] J.R. Willis, Hertzian contact of anisotropic bodies, *Journal of the Mechanics and Physics of Solids*. 14 (1966) 163–176. doi:10.1016/0022-5096(66)90036-6.

- [19] Z. Baicheng, L. Xiaohua, B. Jiaming, G. Junfeng, W. Pan, S. Chen-nan, N. Muiling, Q. Guojun, W. Jun, Study of selective laser melting (SLM) Inconel 718 part surface improvement by electrochemical polishing, *Materials and Design*. 116 (2017) 531–537. doi:10.1016/j.matdes.2016.11.103.
- [20] S.J. Hessel, W. Voice, A.W. James, S.A. Blackham, C.J. Small, M.R. Winstone, Nickel Alloy for Turbine Engine Component, US Patent 6132527, 2000.
- [21] W.C. Oliver, G.M. Pharr, An improved technique for determining hardness and elastic modulus using load and displacement sensing indentation experiments, *Journal of Materials Research*. 7 (1992) 1564–1583. doi:10.1557/JMR.1992.1564.
- [22] W.C. Oliver, G.M. Pharr, Measurement of hardness and elastic modulus by instrumented indentation: Advances in understanding and refinements to methodology, *Journal of Materials Research*. 19 (2004) 3–20. doi:10.1557/jmr.2004.19.1.3.
- [23] W. Hermann, H.G. Sockel, J. Han, A. Bertram, Elastic properties and determination of elastic constants of nickel-base superalloys by a free-free beam technique, in: *Superalloys*, TMS, Champion, Pennsylvania, 1996: pp. 229–238.
- [24] X. Zhang, P.R. Stoddart, J.D. Comins, A.G. Every, High-temperature elastic properties of a nickel-based superalloy studied by surface Brillouin scattering, *Journal of Physics: Condensed Matter*. 13 (2001) 2281–2294. doi:10.1088/0953-8984/13/10/320.
- [25] J.F. Nye, *Physical Properties of Crystals: Their Representation by Tensors and Matrices*, Clarendon Press, Oxford, 1957.



- [26] J. Han, A. Bertram, J. Olschewski, W. Hermann, H.G. Sockel, Identification of elastic constants of alloys with sheet and fibre textures based on resonance measurements and finite element analysis, *Materials Science and Engineering A*. 191 (1995) 105–111. doi:10.1016/0921-5093(95)80008-5.
- [27] H.T. Pang, M.C. Hardy, N. Hide, I.M. Wilcock, M.B. Henderson, P.A.S. Reed, Comparison of fatigue crack propagation in nickel base superalloys RR1000 and Udimet 720Li, *Materials Science and Technology*. 32 (2016) 22–39. doi:10.1179/1743284715Y.0000000060.
- [28] C. Zener, *Elasticity and Anelasticity of Metals*, University of Chicago Press, Chicago, 1948.
- [29] T. Gnäupel-Herold, P.C. Brand, H.J. Prask, Accessing the elastic properties of cubic materials with diffraction methods, *Proceedings of the Denver X-Ray Conference*. (1998) 464–470.
- [30] A. Bolshakov, G.M. Pharr, Influences of pileup on the measurement of mechanical properties by load and depth sensing indentation techniques, *Journal of Materials Research*. 13 (1998) 1049–1058. doi:10.1557/JMR.1998.0146.